Korean J. Chem. Eng., 37(2), 358-365 (2020)
DOI: 10.1007/s11814-019-0425-5

pISSN: 0256-1115
eISSN: 1975-7220

Trisodium citrate-assisted synthesis of BiOBr nanostructure catalyst for efficient activity under visible light

Weiming Zhou*, Yifan Jiang*, Shichang Sun*, Mingxin Zhang*, Ibrahim Lawan*, Gerard Franklyn Fernando*,*, Liwei Wang**,****,†, and Zhanhui Yuan*,†**

*College of Materials Engineering, Fujian Agriculture and Forestry University, Fuzhou 350002, China
**Fujian Key Laboratory of Novel Functional Textile Fibers and Materials (Minjiang University), Fuzhou 350108, China
***School of Metallurgy and Materials, University of Birmingham, B15 2TT, UK
****Ocean College, Minjiang University, Fuzhou 350108, China
(*Received 20 August 2019 • accepted 8 November 2019*)

Abstract−A simple one step wet-chemical method assisted by trisodium citrate was employed in the synthesis of BiOBr applied as a photocatalyst. Photocatalytic activity of the BiOBr was investigated for the degradation of Rhodamine B (RhB) dye under visible light irradiation (λ>420 nm). The results indicated that trisodium citrate is more favorable to the formation of hierarchical architectures and reduces the particle size of BiOBr photocatalyst. BiOBr with hierarchical architectures exhibiting significantly higher catalytic activity than that with ordinary nanostructure. The significant improvement could be attributed to the high specific surface area (24.14 $m^2 \cdot g^{-1}$), average pore sizes (34.09 nm) and average pore volume (0.24 $cm^3 \cdot g^{-1}$).

Keywords: BiOBr, Trisodium Citrate, Visible Light Photocatalytic Activity, Hierarchical Architectures, High Specific Surface Area

INTRODUCTION

Significant attention continues to be paid to the preparation and performance of photocatalytic materials, such as TiO_2 [1], ZnO [2] and Bi_2O_3 [3]. These classes of materials have been used for the removal of pollutants from the environment [4], hydrogen gas production by splitting water [5] and the reduction of CO_2 to produce hydrocarbon fuels [6]. However, most of them are activated by ultraviolet light (UV). Since solar radiation on the earth's surface consists of about 5% UV (300-400 nm), 43% visible (400-700 nm) and 52% infrared (700-2,500 nm) [7-9], there is significant merit in developing photocatalytic materials that can be activated by visible light.

BiOX (Bismuth-based oxyhalides, X=F/Cl/Br/I) are an important class of group V-VI-VII ternary compounds, of which the crystallize structure comprises the $[Bi_2O_2]^{2+}$ layer and interleaved X^- double slabs. These materials have optical transition properties and open crystalline structures due to the strong intra-layer covalent bonds and weak inter-layer van der Waals bonds [10]. Among these classes of BiOX nanomaterials, BiOBr powders show superior visible light-activated photocatalytic activity for degrading pollutants [11]. However, they are mainly prepared by hydrothermal and solvothermal methods involving high temperature and pressure, expensive raw and processed material, and long reaction time [12]. As such, preparing the BiOBr photocatalyst with high photocatalytic activity at mild condition would be a welcome development.

Photocatalytic activity is related to the particle size and the morphology of the photocatalysts [13-15]. Compared with bulk catalysts, the specific surface area increases significantly with the decrease of catalyst particle size [16,17], and it is also advantageous to reduce the recombination of photogenerated electrons-hole pairs and transfer them to the surface of catalysts to degrade target molecules [18]. Various researchers have reported that increasing the pore volume and average pore diameter will lead to the improvement of photocatalytic activity for organic pollutant degradation [19,20]. The preparation conditions have been used to control the particle size and morphology of photocatalysts including temperature and time, template and template-free, and so on [21-23]. Hierarchical structures have the advantages of nanounits, high specific surface area, abundant interspaces, which are beneficial to improving the photocatalytic activity of photocatalyst [24]. With reference to the synthesis of photocatalysts with hierarchical architectures, trisodium citrate molecule possessing multiple coordination functional groups (-COO- and -OH) has been used as structure-directing agent [25-29]. However, most of these hierarchical architectures form flower-like or nest-like structures under acidic or neutral conditions, and the average size of the microstructures ranges from 0.8 to 1.5 μm [30,31].

In this study, BiOBr nanostructure photocatalyst with hierarchical architectures was synthesized at room temperature in a simple one-step wet-chemical method, using trisodium citrate to assist synthesis and sodium hydroxide to regulate the pH value of reaction system. It has been reported that the functional groups of trisodium citrate can complexate with metal ions (metal-citrate complex) in the acidic condition, while it is not stable in the alkaline condition [32]. Also, controlled particle size by reaction conditions can extend to the synthesis process of the other nanomaterial. Interestingly, our findings reveal that trisodium citrate is beneficial to the synthesis

†To whom correspondence should be addressed.
E-mail: zhanhuiyuan@fafu.edu.cn, wlw@mju.edu.cn

of BiOBr nanostructures with high photocatalytic activity, and its specific surface area is higher than that ordinary BiOBr nanostructures photocatalyst without trisodium citrate-assisted synthesis.

EXPERIMENTAL

1. Synthesis of the Photocatalyst

1.2 mmol bismuth nitrate ($Bi(NO_3)_3 \cdot 5H_2O$) and 2.4 mmol trisodium citrate ($Na_3C_6H_5O_7 \cdot 2H_2O$) were dissolved in 15 mL of 2 mol/L nitric acid (HNO_3). The solution was stirred for 10 minutes to obtain solution I. Solution II was made by adding 0.14 g sodium bromide (NaBr) and 0.30 g sodium hydroxide (NaOH) into 15 mL deionized water. Solution I was added dropwise to solution II at 1.7 mL/min via a peristaltic pump. The suspension was stirred at room temperature for 30 minutes, and the mixture was centrifuged and washed several times with deionized water and ethanol. The final procedure involved drying the solution at 80 °C in an air-circulating oven to obtain a solid powder that was coded as BOB-RT.

The sample prepared without trisodium citrate was coded as BOB-RT-NT. The sample synthesized without adding NaOH was denoted as BOB-RT-NS, the powder made without the addition of trisodium citrate and NaOH was denoted as BOB-RT-NTS. The preparation process and strategy are depicted in Fig. S1.

2. Characterization

The crystal structure was characterized by powder X-ray diffraction (XRD) with a BRUKER D8 ADVANCE diffractometer equipped with Cu-Ka source. Fourier transform infrared (FT-IR) spectra were obtained using a Thermo Scientific Nicolet iS10 spectrometer in the spectral range covering 4,000-400 cm^{-1}. Field emission scanning electron microscope (SEM) images were collected with Hitachi Regulus8100. Transmission electron microscopy (TEM) and High-resolution TEM (HRTEM) micrographs were obtained via a FEI Talos F200X TEM microscope. Ultraviolet-visible diffuse reflectance (UV-Vis DRS) spectra were recorded on a UV-Vis spectrophotometer (Shimadzu UV 2600), where $BaSO_4$ was used as the reference. The surface areas, average pore diameter, pore volumes and pore size distributions were obtained from nitrogen adsorption-desorption isotherms using of ASAP 2020 Plus HD88 instrument.

3. Photo-electro-chemical Measurement

The photo-electro-chemical properties were recorded on a three-electrode electro-chemical workstation (CS310H, Wuhan CorrTest Instrument Co., Ltd., China). A 300 W xenon lamp with a 420 nm cutoff filter (FX300, Beijing Perfectlight Technology Co., Ltd., China) was the visible light source. The prepared samples were mixed with Nafion solution (D520, DuPont Co., Ltd., America) to form slurry and then deposited on a 1×2 cm indium-tin-oxide (ITO)-coated glass, and it served as the working electrode. A platinum plate, Ag/AgCl (saturated KCl) and 0.5 M Na_2SO_4 were used as the counter electrode, reference electrode and electrolyte, respectively.

4. Photocatalytic Reaction

The photocatalytic degradation of RhB dye solution was studied under visible light (λ>420 nm) irradiated from a 300 W xenon lamp (CEL-HXUV300, Beijing CEAULIGHT Co., Ltd., China). 20 mg of the photocatalyst was added to 100 mL of 30 mg/L RhB dye solution. Prior to illumination, the suspension was placed in the dark and stirred with a magnetic stirrer for 30 minutes. In the case of the photocatalytic reaction, the suspension was transferred from its light-tight environment and irradiated with visible light while subjected to constant stirring. 2 mL of the suspension was removed at selected time intervals and the absorbance spectra and the concentration of RhB solution were obtained using UV/visible spectroscopy as described previously. After the previous degradation process, the suspension was centrifuged, washed severally with deionized water and ethanol, dried and used in the subsequent degradation process. The catalyst dosage and dye concentration were the same as those used in the previous degradation processes.

RESULTS AND DISCUSSION

1. XRD and FT-IR

Fig. 1(a) shows the XRD pattern of the prepared nanostructured BiOBr photocatalyst. All the characteristic diffraction peaks were in accordance with tetragonal phase for BiOBr (JCPDS Card No. 01-073-2061). The diffraction peaks are observed at 2θ values of 10.9°, 21.9 °, 25.2°, 31.7°, 32.3°, 39.4°, 46.3° 57.2°, corresponding to the crystal planes of {001}, {002}, {011}, {012}, {110}, {112}, {020}, {212}, respectively [6]. The BOB-RT, BOB-RT-NS and BOB-RT-NT samples show diffraction peak intensity ratios of 012/001, 110/001 and 020/001 are greater than 1. However, the BOB-RT-NTS photocatalyst shows that the diffraction peaks intensity ratio for

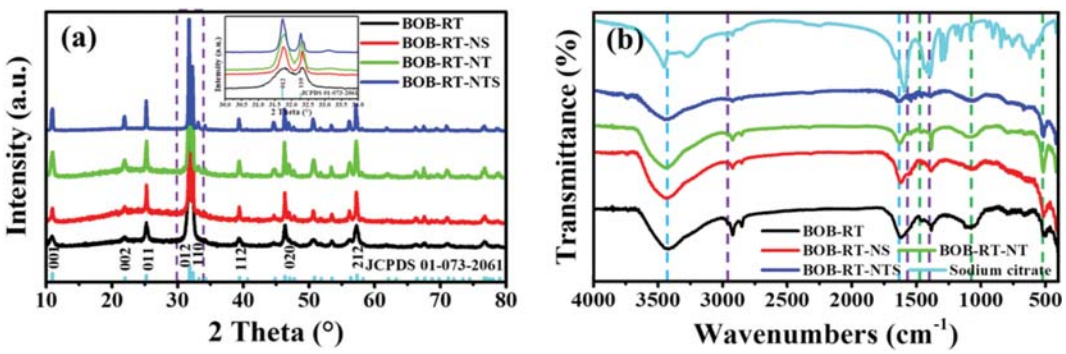

Fig. 1. XRD pattern (inset: diffraction peak position of {012} and {110} in the range from 30 to 34°) (a) and FT-IR spectra of the prepared samples and trisodium citrate (b).

020/001 is close to 1 (Fig. S2). This implies that the BiOBr nanostructure photocatalyst with preferential exposed {010} crystal facet was prepared with trisodium citrate and NaOH [33]. It has been reported that under visible light, the photocatalytic efficiency of {010} crystal facet highly exposed catalyst is higher than that of {001} crystal facet, which the intra-electric field of BiOBr materials is along the [001] direction, and the surface energy of {001} facets is much lower than other facets [34,35]. The width of the diffraction peak increases obviously at 31.7° and 32.3° with the addition of trisodium citrate and NaOH, respectively (inset in Fig. 1(a)). According to Scherrer's equation, this shows that the crystallite size of BiOBr crystal in BOB-RT sample decreases.

The FT-IR spectra of the prepared samples and trisodium citrate are shown in Fig. 1(b). The broad bands around 3,440 cm^{-1} and 1,620 cm^{-1} are assigned to the stretching and flexural vibrations of -O-H from adsorbed water or trisodium citrate [36]. The two absorption peaks located at 1,452 cm^{-1} and 1,051 cm^{-1} are attributed to the asymmetry and symmetric stretching vibration of Bi-Br bond [37]. The peaks below 520 cm^{-1} correspond to the symmetric stretching vibration of Bi-O bond [38]. The small peak at 2,963 cm^{-1} indicates the stretching vibration of the -C-H, while peaks at 1,590 cm^{-1} and 1,390 cm^{-1} are attributed to the -COO- groups [39]. The peaks of -C-H and -COO- groups observed in BOB-RT and BOB-RT-NS are in good agreement with that of trisodium citrate [40].

2. SEM and HRTEM

The particle size and morphology of the catalysts have a significant impact on the photocatalytic activity with regard to the degradation of target molecules [41]. The particle size of the BOB-RT-NTS shown in Fig. 2(a) is obviously bigger than that for BOB-RT-NS, BOB-RT-NT and BOB-RT shown in Fig. 2(b), (c) and (d), respectively. The morphology of the BiOBr photocatalyst was investigated by SEM where it was observed that it has flake structure with a larger ratio of diameter-to-thickness when trisodium citrate and NaOH were not be used. The photocatalyst synthesized with sodium citrate assistance without NaOH for adjusting pH showed a flower-like structure (Fig. 2(b)), which is similar to the results in the literature [31]. In alkaline condition, the particle size of photocatalyst prepared without the assistance of trisodium citrate decreases,

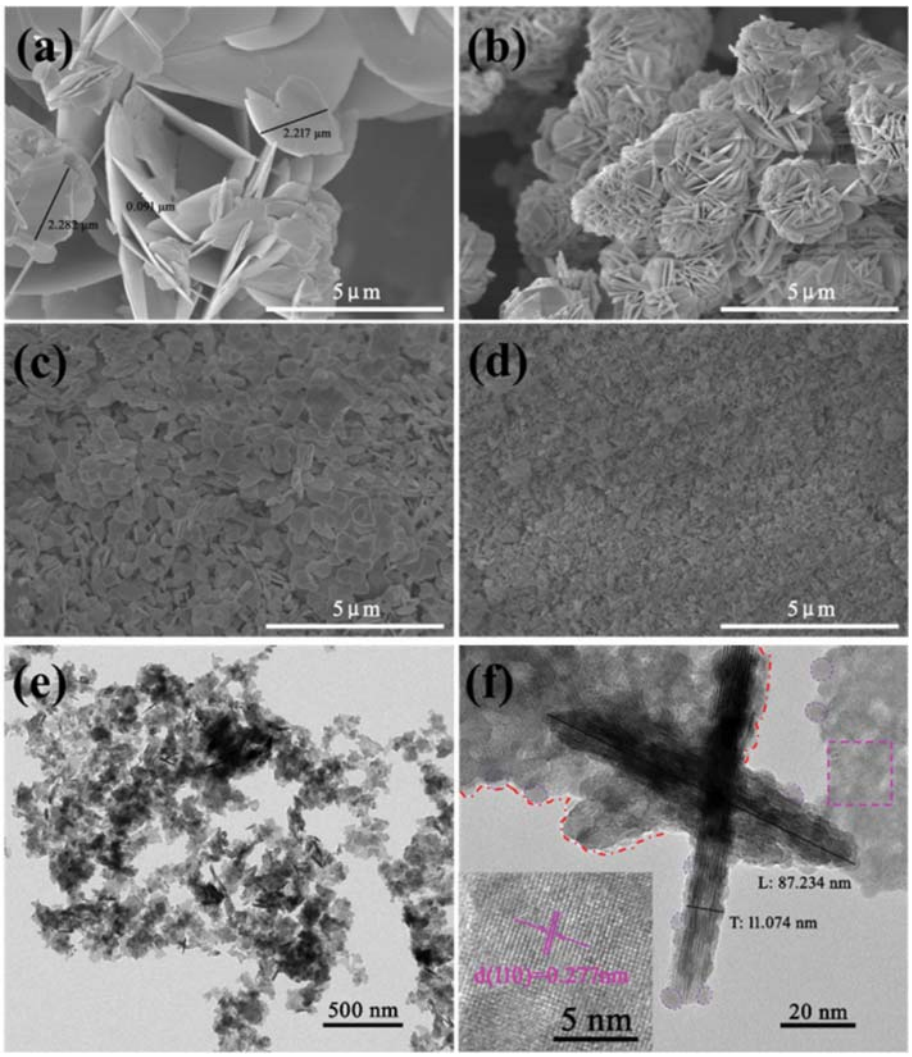

Fig. 2. SEM images of BOB-RT-NTS (a), BOB-RT-NS (b), BOB-RT-NT (c), BOB-RT (d), TEM (e) and HRTEM (f) images of BOB-RT (inset: the {110} facet of BiOBr).

as shown in Fig. 2(c). However, comparing the synergistic effect of trisodium citrate and NaOH for adjusting pH, it can be seen that the particle size of other samples are significantly larger (Fig. 2(d)). This indicates that the particles sizes of BiOBr photocatalyst are greatly dependent on the trisodium citrate and NaOH. This result corroborates the earlier on findings from the XRD pattern (inset in Fig. 1(a)). Furthermore, the EDX spectra of BOB-RT, BOB-RT-NS, BOB-RT-NT and BOB-RT-NTS show that the atomic content ratios of O, Br and Bi in all samples are very close to 1 : 1 : 1 (Fig. S3).

The morphology and microstructure of BOB-RT were inspected further by TEM and HRTEM. According to the TEM analysis of BOB-RT shown in Fig. 2(e), BiOBr exhibited irregular nanosheets morphology. HRTEM analysis of the BOB-RT shown in Fig. 2(f) gave ad-spacing of 0.277 nm (inset in Fig. 2(f)) and this corresponds to the {110} crystal facet of BiOBr [19,20]. The BiOBr nanostructured photocatalyst obtained with trisodium citrate and NaOH mainly consists of thin films with a lateral and thickness dimensions of about 87 nm and 11 nm, respectively. In addition, as shown in Fig. 2(f), some nanoscale layered deposit sediments can be observed on the surface of BiOBr thin films, forming a hierarchical structure that is beneficial to the increase of specific surface area.

3. Nitrogen Adsorption-desorption Isotherms

Fig. 3 shows the nitrogen adsorption-desorption isotherms for the prepared samples. The isotherms are representative of "type-IV" with type-H3 hysteresis loops [34]. The results show the presence of slit-like mesopores in the samples where their formation has been attributed to the accumulation of nanosheets [26,37,42,43]. Moreover, with the BOB-RT, the mesoporous distribution was concentrated at about 2.2 nm (inset in Fig. 3). This result reveals that the nanosheet was the self-assembly of small nanoplate in the formation of hierarchical architectures [39,43], and the result consistent with the HRTEM images is presented in Fig. 2(f).

The results listed in Table 1 show how trisodium citrate and NaOH significantly affected the BET specific surface area and pore characteristic of the samples. The BET specific surface area, average pore sizes and pore volume of the BOB-RT sample were 24.14 m^2/g, 34.09 nm and 0.24 $cm^3 \cdot g^{-1}$, respectively. This is significantly higher than that observed for BOB-RT-NS, BOB-RT-NT and BOB-RT-NTS. This demonstrates that trisodium citrate-assisted process flows by the NaOH treatment for the adjustment of the pH value are of significant importance towards obtaining BOB-RT sample with high specific surface areas, and the aggregation of nanosheets is more favorable to the formation of macropore. In general, a large specific surface area is conducive to adsorbing more of the target molecule that is to be degraded, and this results in a higher photocatalytic activity [44].

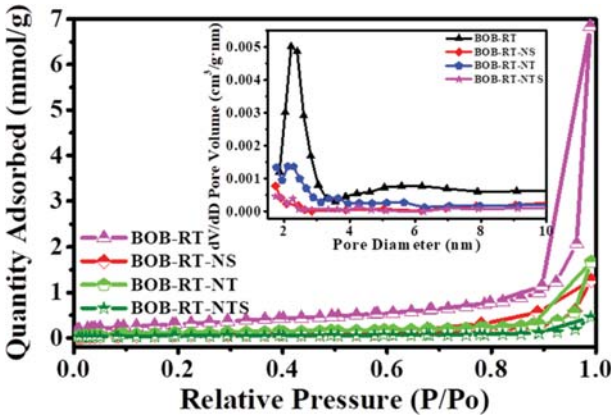

Fig. 3. Nitrogen adsorption-desorption isotherms of the prepared samples (inset: pore size distribution).

4. UV-vis Spectroscopy

The UV-visible spectra of the photocatalyst were analyzed by UV-Vis DRS spectrometer as depicted in Fig. 4(a). The range of

Table 1. BET surface areas and pore characteristics of the prepared samples

Sample	$S_{p(BET)}$ ($m^2 \cdot g^{-1}$)	BJH adsorption average pore diameter (nm)	BJH adsorption cumulative volume of pores ($cm^3 \cdot g^{-1}$)
BOB-RT	24.14	34.09	0.24
BOB-RT-NS	6.10	30.23	0.044
BOB-RT-NT	8.46	27.04	0.058
BOB-RT-NTS	3.19	26.27	0.016

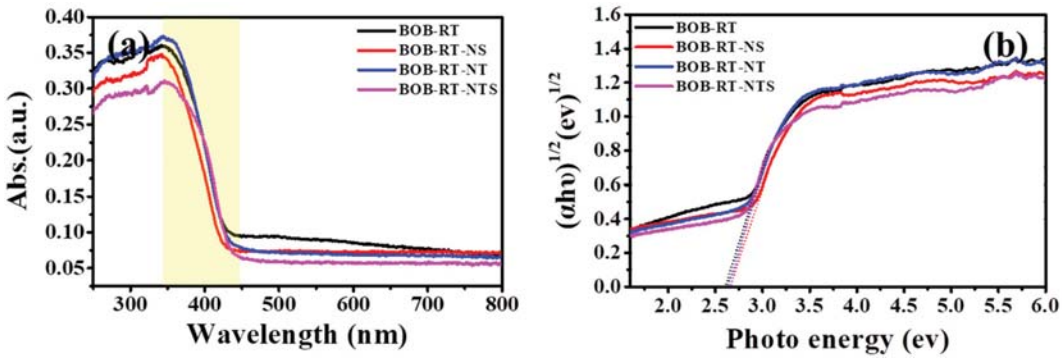

Fig. 4. UV-vis diffuse reflectance spectra (a) and plots of $(\alpha h\nu)^{1/2}$ vs $h\nu$ (b) of the prepared samples.

the optical absorption edges of all samples was in the range 340-450 nm, and it resulted in the samples having a slightly yellow tinge. The band gap energy (E_g) was near an optical absorption edge according to the Eq. (1):

$$(\alpha h\nu)^{1/2}=A(h\nu-E_g) \quad (1)$$

where α, h, ν and A are the absorption coefficient, Planck constant, frequency of the light and a proportionality constant, respectively [23,34,45-47]. Plots of $(\alpha h\nu)^{1/2}$ versus hν are shown in Fig. 4(b), and the E_g values of the prepared samples are estimated to be BOB-RT (2.62 eV), BOB-RT-NS (2.67 eV), BOB-RT-NT (2.63 eV) and BOB-RT-NTS (2.67 eV). This subtle alteration may be attributed to the influence of the particle size. The amplitude of atomic vibration and the inter-atomic spacing was correspondingly enlarging with the decrease of particle size, and then the E_g had a small red shift [48].

Moreover, as shown in Fig. 4(a), a broad and relatively weak peak centered at 550 nm indicates that oxygen vacancies exist in the BOB-RT sample [49,50]. It is generally believed that the reduction of particle size can produce more oxygen vacancies and inhibit the recombination of electron-hole pairs, thus promoting the photocatalytic process [51,52].

5. Photo-electro-chemical Measurements

The ability of photo-generated electron-hole pairs (charge carriers) separation and transport is determined by the particle size and morphology [41], which can be studied by photo-current experiments. The higher the photocurrent density of the transient photocurrent response, the more efficient the electron hole separation and the higher the photocatalytic activity [53]. As can be seen in Fig. 5(a), BOB-RT exhibited a higher photocurrent density than other samples when irradiated with visible light. This indicates that BOB-RT has a more effective electron-hole pair separation and it leads

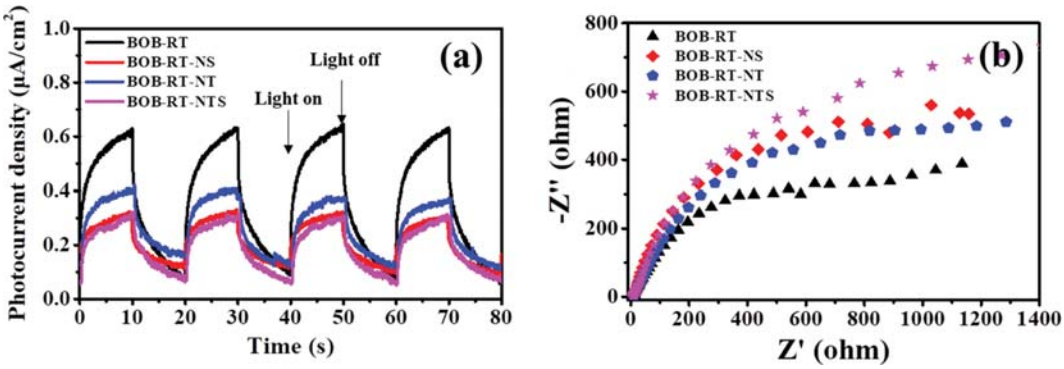

Fig. 5. Transient photocurrent responses under visible light irradiation (a) and EIS Nyquist plots of the prepared samples (b).

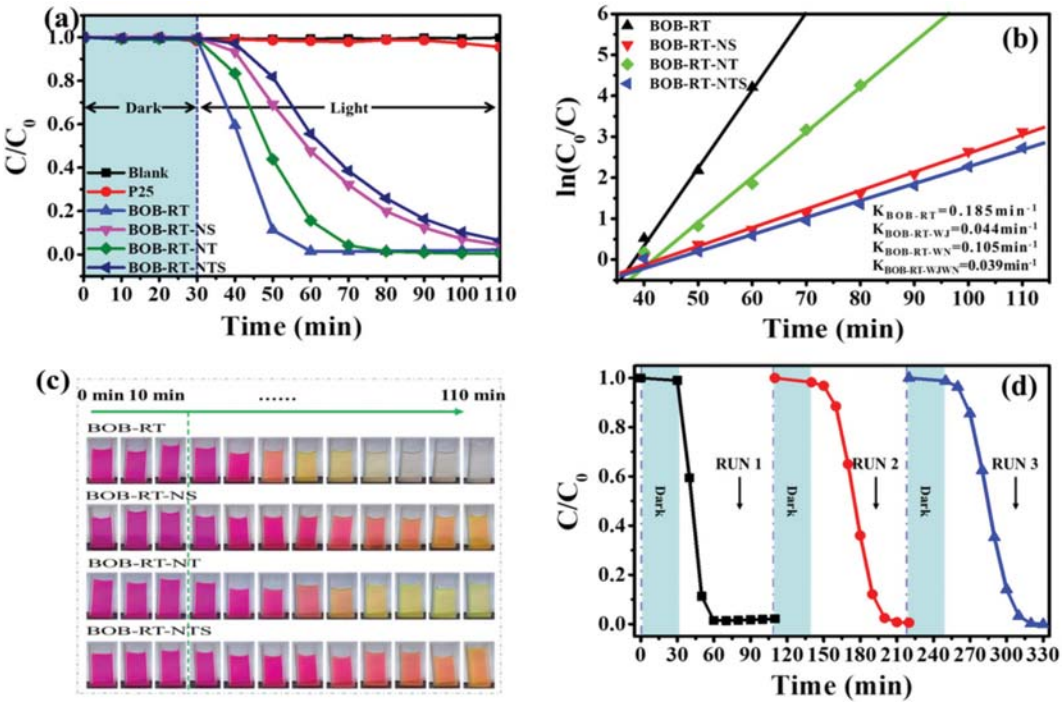

Fig. 6. Photocatalytic activity (a) and kinetics (b) of the prepared samples for the degradation of RhB, photos of the RhB solution in cuvette (quartz absorption cells) (c) and RhB degradation of BOB-RT in three cyclings (d).

to a higher photocatalytic activity. This conclusion is consistent with a previous observation [54]. Fig. 5(b) represents the EIS Nyquist plots of the samples. The arc radius of BOB-RT is smaller than that observed for the other samples. This demonstrates that BOB-RT possesses a higher efficiency [55]. Overall, reducing the particle size of the photocatalyst can improve the separation of photo-generated electron-hole pairs and enables a rapid charge carriers transfer efficiency, which will enhance the photocatalytic activity.

6. Photocatalytic Activity

The ratio of the RhB solution concentration (C) to its initial concentration (C_0) with the degradation time at 552 nm as well as the pseudo-first-order reaction kinetics (k) are shown in Fig. 6(a) and 6(b), respectively. Under irradiation with visible light, the control test (without catalyst) had no photocatalytic activity. A weak degradation of the RhB solution was observed with TiO_2 (P25) catalyst. The photocatalytic efficiency of the catalyst prepared with trisodium citrate and NaOH shows a remarkable improvement. In the presence of BOB-RT, when the RhB solution was irradiated visible light for 30 minutes, about 98.52% RhB was degraded. Furthermore, the calculated rate constants for the degradation of RhB for different catalyst are: 0.184 min^{-1} for BOB-RT; 0.044 min^{-1} for BOB-RT-NS; 0.105 min^{-1} for BOB-RT-NT; and 0.039 min^{-1} for BOB-RT-NTS. Under irradiation with visible light, BOB-RT exhibited significantly higher photocatalytic activity than other photocatalysts, and this is attributed to particle size and microstructure. The data of active species trapping experiment show that the main active species in RhB photodegradation process are mainly photogenerated holes (Fig. S4). As the degradation reaction proceeds, the photographs of RhB solution in the cuvette (quartz absorption cells) are shown in Fig. 6(c), the RhB dye is deethylated in a step-by-step manner [56], and the color of the solution changes from the initial red to the light green yellow, and finally becomes colorless, as confirmed by the UV-vis absorption spectra of RhB solution at different irradiation time (Fig. S5).

The recyclability and photocatalytic stability of BOB-RT was investigated and the results are presented in Fig. 6(d). Degradation of RhB under 30 min was carried out during the first cycle, while about 60 min was used during the second and third cycle processes. The nitrogen adsorption-desorption isotherm and summary properties of BOB-RT after first cycle (BOB-RT-1st) are displayed in Fig. S6 and Table S1. The photocatalytic efficiency of the recycled BiOBr became lower, which was attributed to the average pore sizes and pore volume having sharp reduction after first cycle, may be due to the photocatalytic degradation of trisodium citrate between nanosheets in the sample with BiOBr [57] and then the degradation efficiency of BOB-RT in the second cycling was reduced. On the other hand, the BET specific surface area of the sample did not change greatly, so it can be seen that the average pore sizes and pore volume of the sample also have a great impact on the photocatalytic performance of the material.

Trisodium citrate contains three carboxyl groups and one hydroxyl group. Therefore, it can provide coordinating sites to form a stable coordination with metal ions in the acidic condition and selectively bind to specific crystallographic surfaces to control crystal growth [30,58]. The growth of BiOBr nanoparticles was restricted due to Bi^{3+} being anchored by trisodium citrate. Moreover, the electrostatic repulsion between carboxyl and hydroxyl groups on the surface of BiOBr mesocrystal makes it does disperse uniformly in water [27], the hierarchical architectures consists self-assembly of nanoparticles with mesocrystal growth [12,59], which have many other reports on this kind of method to synthesis hierarchical architectures like BOB-RT-NS. On the other hand, in the absence of trisodium citrate, BiOBr crystallization and growth rate will be very fast due to no chelating effect existing [60]. Others, when bismuth source was added to the reaction system with higher pH value, it is easy to decompose, a large number of BiOBr crystal seeds will be formed quickly, which is not conducive to the growth of particles, so the particles are smaller [61], such as the sample BOB-RT-NT. At the same time, citric acid anion can be adsorbed on the surface of nanoparticles or nanoplates, which also can delay the formation and crystal growth of BiOBr nanoparticles and dramatically inhibit their further growth, forming a hierarchical structure [62,63]. Overall, trisodium citrate-assisted synthesis and NaOH-adjusted pH value of the reaction system are more conducive to the particle size reduction and the formation of hierarchical architectures, to prepare the BOB-RT sample, thus affecting the efficiency of photocatalytic degradation of organic pollutants. More importantly, the method adjusted the particle size, specific surface area, average pore sizes and pore volume by controlling the dosage of trisodium citrate and NaOH; it can be extended to the synthesis of other nanomaterials. The schematic illustration of the morphology evolution of the BOB-RT, BOB-RT-NS, BOB-RT-NT and BOB-RT-NTS is shown in Fig. 7.

CONCLUSIONS

BiOBr photocatalyst with hierarchical architectures was synthesized at room temperature using a simple one step wet-chemical method with trisodium citrate. The catalyst exhibited significantly higher catalytic activity in the degradation of RhB dye than the ordinary BiOBr photocatalyst synthesized without assistance of trisodium citrate under visible light. The result revealed that trisodium

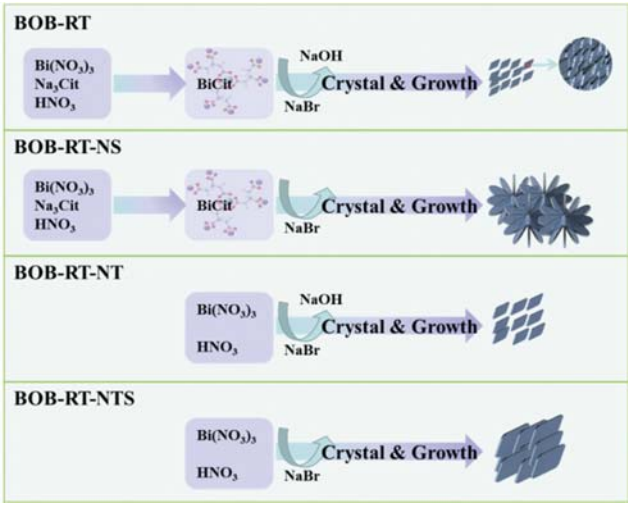

Fig. 7. Schematic of the morphology evolution of the prepared samples.

citrate is advantageous in the formation of photocatalyst with small particle and special morphology as well as high BET specific surface area, average pore sizes, average pore volume. The hierarchical architectures also play a vital role in improving photocatalytic activity.

ACKNOWLEDGEMENTS

This work is supported by the Open Project Program of Fujian Key Laboratory of Novel Functional Textile Fibers and Materials (Minjiang University), China (No. FKLTFM1708), the Fujian Engineering Research Center of New Chinese lacquer Material (Minjiang University), China (No. 323030010301), the authors humbly acknowledge international funding provided by Fujian Agriculture and Forestry University (No. KXB16001A) and the Department of Science and Technology of Fujian Province (No. 2017H6003).

CONFLICT OF INTEREST

The authors have no conflict of interest with regards to the submission and publication of this article.

SUPPORTING INFORMATION

Additional information as noted in the text. This information is available via the Internet at http://www.springer.com/chemistry/journal/11814.

REFERENCES

1. S. J. A. Moniz, S. A. Shevlin, D. J. Martin, Z. Guo and J. W. Tang, *Energy Environ. Sci.*, **8**, 731 (2015).
2. M. Francavilla, A. Pineda, A. A. Romero, J. C. Colmenares, C. Vargas, M. Monteleone, R. Luque and M. Monteleone, *Green Chem.*, **16**, 2876 (2014).
3. Z. F. Bian, J. Zhu, S. H. Wang, Y. Cao, X. F. Qian and H. X. Li, *J. Phys. Chem.* C, **112**, 6258 (2008).
4. R. P. Li, H. J. Ren, W. H. Ma, S. M. Hong, L. Wu and Y. P. Huang, *Catal. Commun.*, **106**, 1 (2017).
5. J. Li, G. M. Zhan, Y. Yu and L. Z. Zhang, *Nat. Commun.*, **7**, 11480 (2016).
6. P. Q. Wang, P. Yang, Y. Bai, T. Chen, X. Shi, L. Ye and X. Zhang, *J. Taiwan Inst. Chem. Engineers*, **68**, 295 (2016).
7. Z. Liu, X. X. Xu, J. Z. Fang, X. M. Zhu, J. H. Chu and B. J. Li, *Appl. Surf. Sci.*, **258**, 3771 (2012).
8. I. Jang, K. E. You, Y. C. Kim and S. G. Oh, *Appl. Surf. Sci.*, **316**, 187 (2014).
9. R. Levinson, P. Berdahl and H. Akbari, *Solar Energy Mater. Solar Cells*, **89**, 351 (2005).
10. K. L. Zhang, C. M. Liu, F. Q. Huang, C. Zheng and W. D. Wang, *Appl. Catal. B: Environ.*, **68**, 125 (2006).
11. Z. S. Liu, B. T. Wu, J. N. Niu, X. Huang and Y. B. Zhu, *Appl. Surf. Sci.*, **288**, 369 (2014).
12. Y. Xu, S. C. Xu, S. Wang, Y. X. Zhang and G. H. Li, *Dalton Trans*, **43**, 479 (2013).
13. M. Shang, W. Z. Wang and L. Zhang, *J. Hazard. Mater.*, **167**, 803 (2009).
14. A. G. Abraham, A. Manikandan, E. Manikandan, S. Vadivel, S. K. Jaganathan, A. Baykal and P. S. Renganathan, *J. Magn. Magn. Mater.*, **452**, 380 (2018).
15. C. P. Sajan, S. Wageh, A. A. Al-Ghamdi, J. Yu and S. Cao, *Nano Res.*, **9**, 3 (2016).
16. H. Y. Jeong, J. H. Lee and K. F. Hayes, *Geochim. Cosmochim. Acta*, **72**, 493 (2008).
17. O. Yamamoto, *Int. J. Inorg. Mater.*, **3**, 643 (2001).
18. J. Li, Y. Yu and L. Z. Zhang, *Nanoscale*, **6**, 8473 (2014).
19. R. S. Yuan, R. B. Guan and J. T. Zheng, *Scripta Materialia*, **52**, 1329 (2005).
20. D. S. Kim, S. J. Han and S. Y. Kwak, *J. Colloid Interface Sci.*, **316**, 85 (2007).
21. H. T. Wang, M. S. Shi, H. F. Yang, N. Chang, H. Zhang, Y. P. Liu, M. C. Lu, D. Ao and D. Q. Chu, *Mater. Lett.*, **222**, 164 (2018).
22. Z. Jiang, F. Yang, G. D. Yang, L. Kong, M. O. Jones, T. C. Xiao and P. P. Edwards, *J. Photochem. Photobiol. A Chem.*, **212**, 8 (2010).
23. H. P. Li, J. Y. Liu, T. X. Hu, N. Du, S. E. Song and W. G. Hou, *Mater. Res. Bull.*, **77**, 171 (2016).
24. Q. C. Liu, D. K. Ma, Y. Y. Hu, Y. W. Zeng and S. M. Huang, *ACS Appl. Mater. Interfaces*, **5**, 11927 (2013).
25. G. Q. Zhang, G. Q. Yang and J. S. Ma, *Cryst. Growth Des.*, **6**, 375 (2006).
26. Q. H. Liang, W. J. Ma, Y. Shi, Z. Li and X. N. Yang, *Crystengcomm*, **14**, 2966 (2012).
27. X. Jiang, F. M. Wang, W. F. Cai and X. B. Zhang, *J. Alloys Compd.*, **636**, 34 (2015).
28. Z. F. Huang, Y. Zhao, Y. H. Song, Y. H. Zhao and J. Z. Zhao, *Colloids Surf., A, Physicochem. Eng. Aspects*, **516**, 106 (2017).
29. S. B. Zhu, X. Tian, J. J. Chen, L. M. Shan, X. L. Xu and Z. W. Zhou, *J. Phys. Chem. C*, **118**, 16401 (2013).
30. K. Zhang, J. Liang, S. Wang, J. Liu, K. X. Ren, X. Zheng, H. Luo, Y. J. Peng, X. Zou, X. Bo, J. H. Li and X. B. Yu, *Cryst. Growth Des.*, **12**, 793 (2012).
31. K. X. Ren, K. Zhang, J. Liu, H. D. Luo, Y. B. Huang and X. B. Yu, *Crystengcomm*, **14**, 4384 (2012).
32. T. Trindade, J. D. P. de Jesus and P. O'Brien, *J. Mater. Chem.*, **4**, 1611 (1994).
33. H. P. Li, T. X. Hu, N. Du, R. J. Zhang, J. Q. Liu and W. G. Hou, *Appl. Catal. B Environ.*, **187**, 342 (2016).
34. X. Y. Xiong, L. Y. Ding, Q. Q. Wang, Y. X. Li, Q. Q. Jiang and J. C. Hu, *Appl. Catal. B Environ.*, **188**, 283 (2016).
35. M. L. Guan, C. Xiao, J. Zhang, S. J. Fan, R. An, Q. M. Cheng, J. F. Xie, M. Zhou, B. J. Ye and Y. Xie, *J. Am. Chem. Soc.*, **135**, 10411 (2013).
36. H. Li, J. Shang, Z. H. Ai and L. Z. Zhang, *J. Am. Chem. Soc.*, **137**, 6393 (2015).
37. W. T. Li, Y. B. Zou, X. Geng, F. Xiao, G. Y. An and D. S. Wang, *Mol. Catal.*, **438**, 19 (2017).
38. Y. Bai, P. Q. Wang, J. Y. Liu and X. J. Liu, *Rsc Adv.*, **4**, 19456 (2014).
39. D. D. Han, P. C. Xu, X. Y. Jing, J. Wang, P. P. Yang, Q. H. Shen, J. Y. Liu, D. L. Song, Z. Gao and M. L. Zhang, *J. Power Sources*, **235**, 45 (2013).
40. W. Y. Li and H. Y. Wu, *Chem. Phys. Lett.*, **686**, S0009261417308072 (2017).

41. F. Vaquero, R. M. Navarro and J. L. G. Fierro, *Appl. Catal. B Environ.*, **203** (2016).
42. K. Li, Y. J. Liang, J. Yang, Q. Gao, Y. L. Zhu, S. Q. Liu, R. Xu and X. Y. Wu, *J. Alloys Compd.*, **695**, 238 (2017).
43. C. T. Yang, W. W. Lee, H. P. Lin, Y. M. Dai, H. T. Chi and C. C. Chen, *Rsc Adv.*, **6**, 40664 (2016).
44. B. Liu, L. M. Liu, X. F. Lang, H. Y. Wang, X. W. Lou and E. S. Aydil, *Energy Environ. Sci.*, **7**, 2592 (2014).
45. J. Yang, Y. J. Liang, K. Li, G. Yang, Y. L. Zhu, S. Q. Liu and W. Lei, *Appl. Surf. Sci.*, **458**, 769 (2018).
46. X. Zhang, Z. H. Ai, F. L. A. Jia and L. Zhang, *J. Phys. Chem. C*, **112**, 747 (2008).
47. Y. Ohko, K. Hashimoto and A. Fujishima, *J. Phys. Chem. A*, **101**, 8057 (1997).
48. X. C. Meng and Z. S. Zhang, *J. Mol. Catal. A Chem.*, **423**, 533 (2016).
49. H. Bai, W. Yi, J. Li, G. Xi, Y. Li, H. Yang and J. Y. Liu, *J. Mater. Chem. A*, **4**, 1566 (2016).
50. S. Patnaik, G. Swain and K. M. Parida, *Nanoscale*, **10**, 5950 (2018).
51. P. Jimlim, T. Bovornratanaraks, W. Chaimayo and S. Pratontep, *Mod. Phys. Lett. B*, **25**, 2399 (2011).
52. A. Younis, D. Chu, Y. K. Kanetio and S. Li, *Nanoscale*, **8**, 378 (2015).
53. Y. G. Xu, Y. Ma, X. Y. Ji, S. Q. Huang, J. X. Xia, M. Xie, J. Yan, H. Xu and H. M. Li, *Appl. Surf. Sci.*, **464**, 552 (2019).
54. Y. Y. Ma, Q. Han, F. X. Wang and J. W. Zhu, *Mater. Res. Bull.*, **101**, 272 (2018).
55. B. F. Xin, Z. Y. Ren, H. Y. Hu, X. Y. Zhang, C. L. Dong, K. Y. Shi, L. Q. Jing and H. G. Fu, *Appl. Surf. Sci.*, **252**, 2050 (2005).
56. K. M. Garadkar, L. A. Ghule, K. B. Sapnar and S. D. Dhole, *Mater. Res. Bull.*, **48**, 1105 (2013).
57. J. M. Meichtry, N. Quici, G. Mailhot and M. I. Litter, *Appl. Catal. B Environ.*, **102**, 454 (2011).
58. P. Y. Song, M. Xu and W. D. Zhang, *Mater. Res. Bull.*, **62**, 88 (2015).
59. L. Zhang, X. F. Cao, X. T. Chen and Z. L. Xue, *J. Colloid Interface Sci.*, **354**, 630 (2011).
60. Y. N. Huo, Y. Jin and Y. Zhang, *J. Mol. Catal. A: Chem.*, **331**, 15 (2010).
61. L. Q. Ye, Y. R. Su, X. L. Jin, H. Q. Xie, F. P. Cao and Z. Guo, *Appl. Surf. Sci.*, **311**, 858 (2014).
62. X. L. Hu, Y. Q. Xu, H. K. Zhu, F. N. Hua and S. F. Zhu, *Mater. Sci. Semicond. Process.*, **41**, 12 (2016).
63. L. X. Fang, B. L. Zhang, W. Li, X. J. Li, T. J. Xin and Q. Y. Zhang, *Superlattices Microstruct.*, **75**, 324 (2014).

Supporting Information

Trisodium citrate-assisted synthesis of BiOBr nanostructure catalyst for efficient activity under visible light

Weiming Zhou*, Yifan Jiang*, Shichang Sun*, Mingxin Zhang*, Ibrahim Lawan*, Gerard Franklyn Fernando*,*, Liwei Wang**,****,†, and Zhanhui Yuan*,†**

*College of Materials Engineering, Fujian Agriculture and Forestry University, Fuzhou 350002, China
**Fujian Key Laboratory of Novel Functional Textile Fibers and Materials (Minjiang University), Fuzhou 350108, China
***School of Metallurgy and Materials, University of Birmingham, B15 2TT, UK
****Ocean College, Minjiang University, Fuzhou 350108, China
(*Received 20 August 2019 • accepted 8 November 2019*)

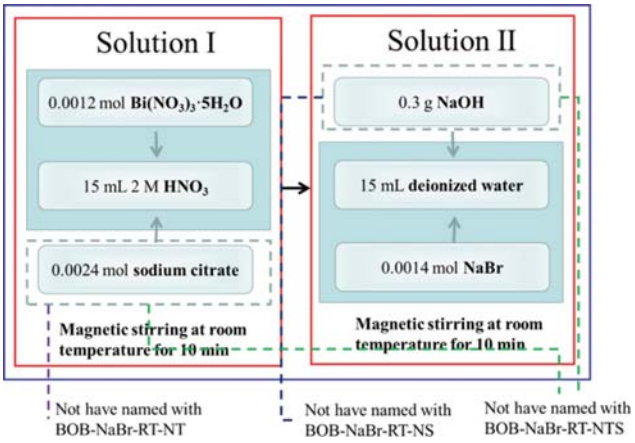

Fig. S1. Preparation process and strategy for prepared samples.

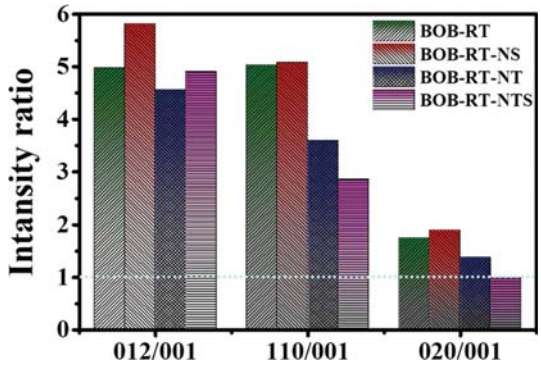

Fig. S2. The intensity ratios of {012}, {110} and {020} to {001}.

The scavengers react with active species when photocatalytic generation, thereby reducing photocatalytic degradation, since trapping agents Ethylene diamine tetraacetic acid (EDTA), methanol (MeOH) and isopropanol (IPA) correspond to photogenerated holes, $\bullet O_2^-$ and •OH, respectively [1-3]. As shown in Fig. S5, EDTA obviously inhibited the degradation efficiency of RhB in all samples, while other trapping agents had weak inhibition, which indicates that the active species for RhB photodegradation process are mainly photogenerated hole.

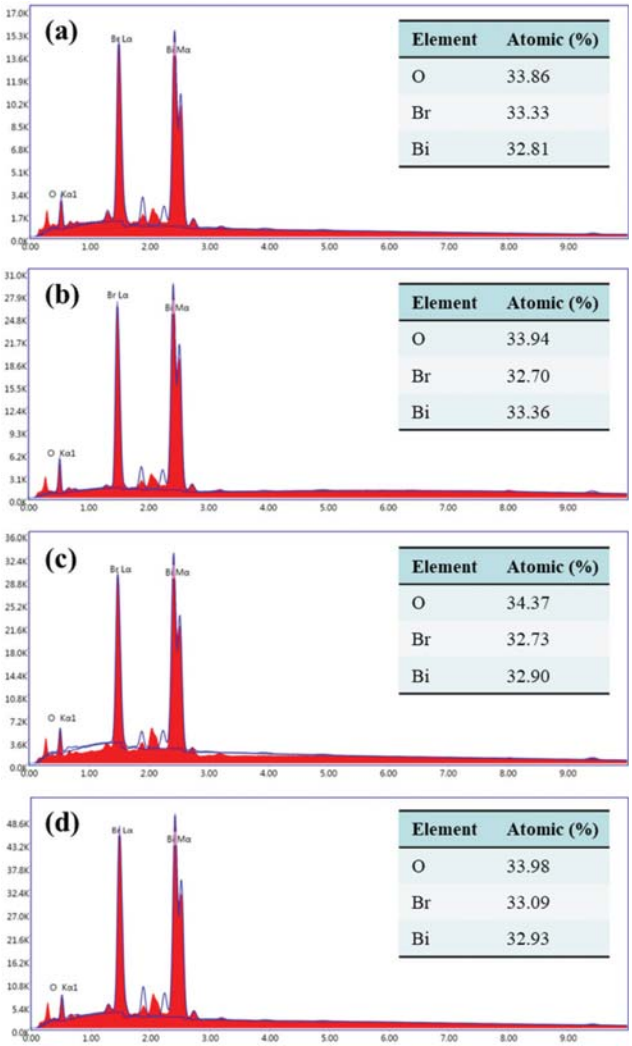

Fig. S3. EDX spectra of BOB-RT (a), BOB-RT-NS (b), BOB-RT-NT (c), BOB-RT-NTS (d).

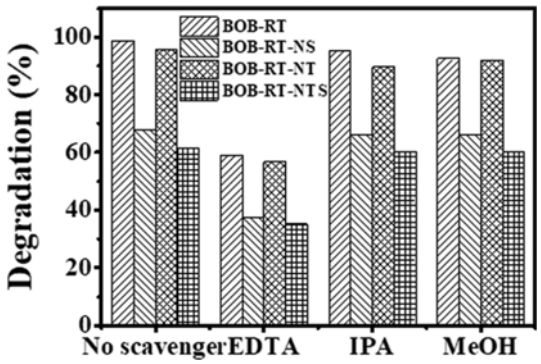

Fig. S4. Active species trapping experiments of RhB photodegradation for the prepared samples.

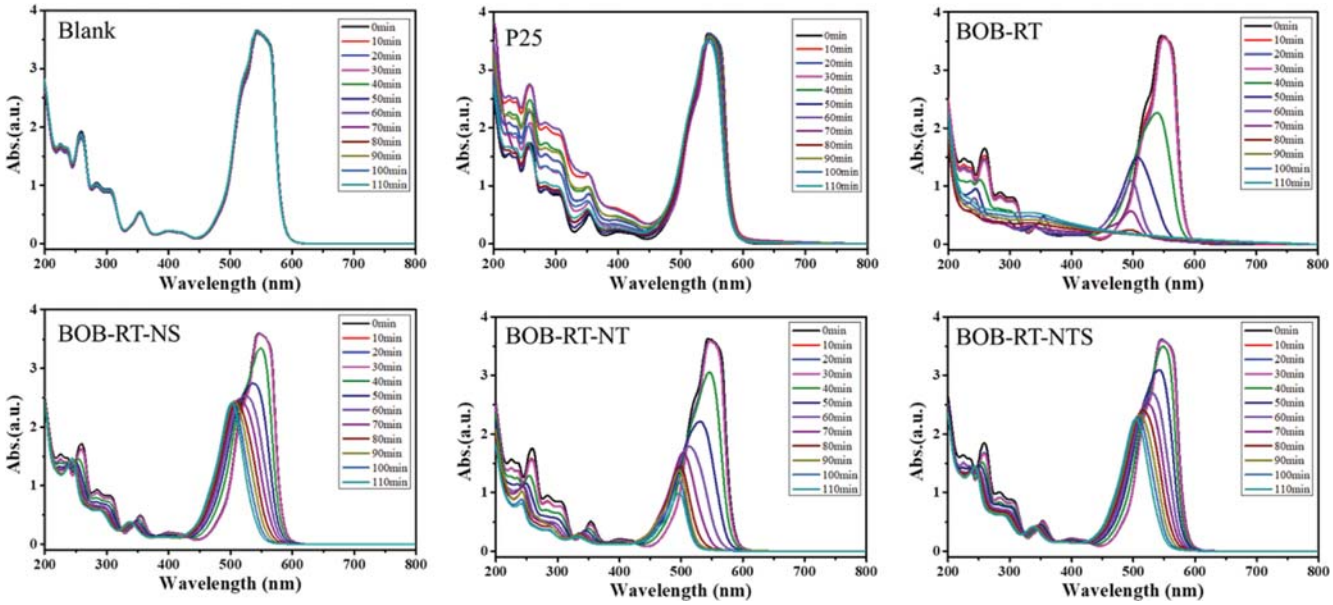

Fig. S5. The UV-vis absorption spectra of RhB at different irradiation time under visible light irradiation.

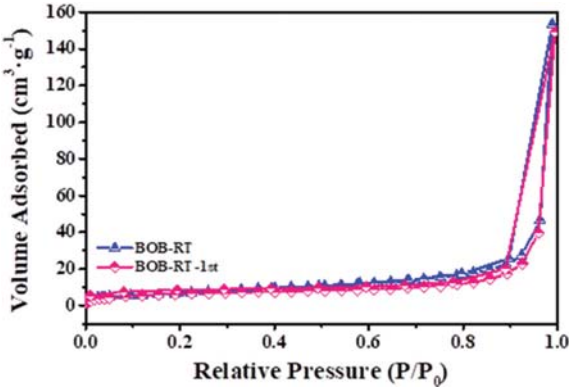

Fig. S6. Nitrogen adsorption-desorption isotherms of BOB-RT and BOB-RT-1st.

Table S1. BET surface areas, average pore diameters and pore volumes of sample after first cycle

Sample	$S_{p(BET)}$ ($m^2 \cdot g^{-1}$)	BJH adsorption average pore diameter (nm)	BJH adsorption cumulative volume of pores ($cm^3 \cdot g^{-1}$)
BOB-RT-1st	23.26	13.48	0.059

REFERENCES

1. X. Y. Xiong, L. Y. Ding, Q. Q. Wang, Y. X. Li, Q. Q. Jiang and J. C. Hu, *Appl. Catal. B: Environ*., **188**, 283 (2016).
2. C. F. Yu, P. Y. Yang, L. N. Tie, S. Y. Yang, S. Y. Dong, J. Y. Sun and J. H. Sun, *Appl. Surf. Sci*., **455**, 8 (2018).
3. H. W. Huang, K. Xiao, Y. He, T. R. Zhang, F. Dong, X. Du and Y. H. Zhang, *Appl. Catal. B: Environ*., **199**, 75 (2016).